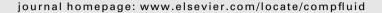
ELSEVIER

Contents lists available at ScienceDirect

# Computers & Fluids





# Influence of the filtering tools on the analysis of two-dimensional turbulent flows

Charles-Henri Bruneau\*, Patrick Fischer

IMB Université Bordeaux 1, INRIA Team MC<sup>2</sup>, CNRS UMR 5251, 351 Cours de la Libération, 33405 Talence, France

#### ARTICLE INFO

Article history: Received 2 March 2007 Accepted 23 January 2008 Available online 22 April 2008

#### ABSTRACT

Numerous direct numerical simulations of soap film flows yield a large amount of data on two-dimensional turbulence. The analysis of such data is very sensitive to the analysis tools and the way they are used. On the one hand, some of the possible errors obtained by a misuse of the analysis tools are reported. On the other hand, a rigorous use of wavelet packets analysis reveals surprising results that slightly differ from the KLB theory for the flow considered. A careful wavelet packets filtering and a good computation of the energy and enstrophy fluxes show the role of the solid rotation vortices and the vorticity filaments to both the inverse energy cascade and the direct enstrophy cascade.

© 2009 Published by Elsevier Ltd.

#### 1. Introduction

The application of wavelets to fluid dynamics has been the topic of many papers [1-4] for the last sixteen years. The main idea developed in these papers is that the vorticity field of a turbulent flow can be easily decomposed in coherent and incoherent parts thanks to an orthogonal wavelet decomposition. The coherent part. corresponding to the strongest wavelet coefficients, is in fact composed by vortices and the so-called incoherent part, corresponding to the weakest coefficients, is mainly composed by vorticity filaments. The part composed by the vorticity filaments is often considered as a background that can be neglected in the computations [4]. However, as it has been shown in [5], these filaments play a fundamental role in the creation of the direct enstrophy cascade, and cannot be removed from the main flow in numerical simulations. It has been shown in [5,6] that the wavelet packets filtering can be successfully applied for analyzing two-dimensional turbulence. This technique allows the highlighting of the two main structures: the vortices and the filaments. The wavelet packets filtering leads to continuous filtered fields and thus avoids the discontinuities that would be created by the filtering method. This is particularly true for the direct filtering proposed by Bensi et al. [7,8] and later developed by Borue [9]. The spurious effects due to this kind of discontinuities created by a direct filtering have been pointed out in [10], and are also discussed in this paper. It is shown in particular that these discontinuities are responsible for the creation of spurious coefficients in Fourier space that alter the corresponding energy and enstrophy spectra. The energy and enstrophy fluxes are also computed to better understand the energy and enstrophy transfer processes through the scales.

The paper is organized as follows. The theoretical background is recalled in Section 2, where we make some remarks about the Danilov inequality. The experimental setup, the mathematical modeling and the filtering process are described in Section 3. The filtering algorithm leading to continuous filtered fields is described but the theory of wavelet packets is not recalled here. In Section 4, windowing methods for the computation of spectra in non periodic domains are discussed. Numerical results showing the effects of the filtering process are given and commented in this section. The results about the energy and the enstrophy spectra and fluxes are given in Section 5. It is shown that the two-dimensional turbulence admits two distinct structures: vortical structures and filamentary structures. The first ones are responsible for the inverse transfers of energy while the second ones are responsible for the forward transfer of enstrophy. A detailed description of the cascades using various injection scales is reported in Section 6. Conclusions and remarks are given in Section 7.

#### 2. The theoretical background

The two-dimensional turbulence, in a finite but periodic domain, is governed by two invariants, the energy and the enstrophy. The mean energy per unit mass E is defined by

$$E \equiv \left\langle \frac{1}{2} |U|^2 \right\rangle = \frac{1}{2} \frac{1}{S(\Omega_L)} \int_{\Omega_L} |U(\mathbf{x})|^2 d\mathbf{x}, \tag{1}$$

where U denotes the velocity vector,  $\mathbf{x} = (x_1, x_2)$  the two-dimensional variable,  $\Omega_L$  the physical domain and  $S(\Omega_L)$  its corresponding surface. If one considers now the velocity U as a L-periodic function, it can be decomposed as a Fourier series

$$U(\mathbf{x}) = \sum_{\mathbf{k}} \hat{U}(\mathbf{k}) e^{\frac{2i\pi \mathbf{k} \cdot \mathbf{x}}{L}}, \quad \mathbf{k} \in \mathbb{Z}^2.$$
 (2)

The low-pass filtered velocity function is then defined as

<sup>\*</sup> Corresponding author.

E-mail address: bruneau@math.u-bordeaux1.fr (C.-H. Bruneau).

 $<sup>^{\</sup>rm 1}$  See also the web page of M. Farge <a href="http://wavelets.ens.fr/PUBLICATIONS/publications.htm">http://wavelets.ens.fr/PUBLICATIONS/publications.htm</a>>.

$$U_K^{<}(\mathbf{x}) = \sum_{|\mathbf{k}| \le K} \widehat{U}(\mathbf{k}) e^{\frac{2i\pi}{L}\mathbf{k}\cdot\mathbf{x}}$$
(3)

and the high-pass filtered velocity function as

$$U_{\mathcal{K}}^{>}(\boldsymbol{x}) = \sum_{|\boldsymbol{k}| > \mathcal{K}} \widehat{U}(\boldsymbol{k}) e^{\frac{2i\pi}{L}\boldsymbol{k} \cdot \boldsymbol{x}}.$$
 (4)

This decomposition of the velocity

$$U(\mathbf{x}) = U_{\kappa}^{<}(\mathbf{x}) + U_{\kappa}^{>}(\mathbf{x}), \tag{5}$$

was used for the first time by Obukhov [11,12]. Introducing this splitting in the Navier–Stokes equations, one obtain a scale-by-scale energy budget equation described by Frisch [13]

$$\partial_t \mathscr{E}(K) + \Pi_E(K) = \mathscr{D}_E(K) + \mathscr{F}_E(K), \tag{6}$$

where

$$\mathscr{E}(K) \equiv \left\langle \frac{1}{2} |U_K^{<}|^2 \right\rangle = \frac{1}{2} \sum_{|\mathbf{k}| \leq K} |\widehat{U}(\mathbf{k})|^2, \tag{7}$$

denotes the cumulative energy,  $\Pi_E(K)$  the energy flux due to the nonlinear terms through the wave number K,  $\mathscr{D}_E(K)$  the energy dissipation, and  $\mathscr{F}_E(K)$  the energy injection. The energy spectrum is then defined by

$$E(k) \equiv \frac{\mathrm{d}\mathcal{E}(k)}{\mathrm{d}k} \tag{8}$$

and the total energy can be rewritten as

$$E = \int_0^\infty E(k) dk. \tag{9}$$

The same splitting can be used in the Navier–Stokes equation written for the vorticity and a scale-by-scale enstrophy budget equation can be obtained

$$\partial_t \mathscr{Z}(K) + \Pi_Z(K) = \mathscr{D}_Z(K) + \mathscr{F}_Z(K), \tag{10}$$

where  $\mathscr{Z}(\mathscr{K})$  denotes the cumulative enstrophy,  $\Pi_Z(K)$  the enstrophy flux,  $\mathscr{D}_Z(K)$  the enstrophy dissipation, and  $\mathscr{F}_Z(K)$  the enstrophy injection. The enstrophy Z can be defined in the same way as the energy

$$Z \equiv \left\langle \frac{1}{2} \left| \omega \right|^2 \right\rangle = \frac{1}{2} \frac{1}{S(B_L)} \int_{B_L} \left| \omega(\mathbf{x}) \right|^2 d\mathbf{x}, \tag{11}$$

where  $\omega = \nabla \times U$  is the vorticity field. The relation between the enstrophy and the enstrophy spectrum is then given by

$$Z = \int_{0}^{\infty} Z(k) \, \mathrm{d}k,\tag{12}$$

where Z(k) stands for the enstrophy spectrum. The energy and enstrophy spectra are linked to each other in Fourier space by the relation

$$Z(k) = \left(\frac{2\pi k}{L}\right)^2 E(k),\tag{13}$$

which reduces to

$$Z(k) = k^2 E(k) \tag{14}$$

in a  $2\pi$ -periodic bounded domain. Using the same notation as Tung and Gkioulekas in [14] this relation can be written in a more general form

$$Z(k) = \Lambda(k)E(k). \tag{15}$$

The fluxes are also related to each other by such a relation

$$\frac{\partial \Pi_Z(k)}{\partial k} = A(k) \frac{\partial \Pi_E(k)}{\partial k}.$$
 (16)

Outside the forcing range, the fluxes should verify the following Danilov inequality:

$$\Lambda(k)\Pi_E(k) < \Pi_Z(k). \tag{17}$$

This inequality is a consequence of the classical frame of the KLB theory in a periodic or infinite domain. However, our experiments consist in the numerical simulation of two-dimensional channel flow perturbed by arrays of cylinders with a no-slip boundary condition in the across-channel direction. A Poiseuille flow is imposed on the entrance section of the channel, and a non reflecting condition is imposed on the exit section. The numerical experiments give a realistic picture of a fluid entering in a channel, perturbed by cylindrical obstacles and exiting the channel. These simulations describe the behavior of a shallow river or a real soap film experiment like in [15-18]. The spectra are computed in a selected square located at the end of the channel. Thus we do not have any periodic condition in any case, and the relations described above between the energy and the enstrophy spectra do not hold anymore. It will be shown in Section 4 that the energy-enstrophy relation numerically diverges in our particular case. This relation is verified only for a short range of frequencies in the middle part of the spectra, approximately between  $k \approx 2L$ (where *L* is the width of the channel) and  $k \approx k_{inj}$ . A detailed study is performed, and the results show that a windowed Fourier transform has to be used for the spectra computations in order to remove the discontinuities created by the boundary conditions.

# 3. The experimental setup, the mathematical modeling and the filtering process

We present in this section the main tools used to compute the two-dimensional turbulent flows and to analyze the flows.

# 3.1. The experimental setup

Many numerical experiments have been performed. All of them consist in the numerical simulation of a two-dimensional channel flow perturbed by an horizontal array of cylinders inducing a 50% blocage. Two vertical arrays of additional cylinders have been added in order to increase the number of merging events, and thus to enhance the inverse energy cascade phenomenon [19]. The injection scale  $k_{ini}$  is given by the diameter of cylinders and so various sizes are considered as shown in Fig. 1 to better capture the inverse energy cascade or the direct enstrophy cascade. The length of the rectangular channel  $\Omega$  is four times its width L and the Revnolds number based on the cylinders diameter is Re = 50,000. This diameter varies from L/8 to L/40 and consequently the injection scale varies from  $k_{inj} = 8$  to  $k_{inj} = 40$ ; the setups plotted in Fig. 1 correspond to  $k_{inj} = 20$  (left) and  $k_{inj} = 8$  (right). As we shall see in the next section, the penalization method is used to solve the flow around the obstacles. Consequently the Brinkman-Navier-Stokes equations are solved in the whole channel  $\Omega$  including the solid obstacles  $\Omega_s$  and the fluid domain  $\Omega_f$ . In all the simulations, the evolution in time of the velocity  $U = (u_1, u_2)$ , of the vorticity  $\omega$  and of the pressure p have been recorded at six monitoring points located on the vertical row  $x_1 = 3L/8$  between 5L/16 and 15L/16. These 1D temporal signals have been analyzed and used to compute the energy spectra reported in [20,21].

The numerical results obtained through such direct numerical simulation can be compared to those obtained by soap film experiments where the flow is perturbed by analogous arrays of small cylinders [19].

# 3.2. The mathematical modeling

Let  $\Omega$  be a rectangular bounded domain in  $\mathbb{R}^2$ . The union of all the solid cylinders is denoted by  $\Omega_s$  and  $\Omega_f = \Omega \setminus \overline{\Omega}_s$  is the incompressible fluid domain in which the Navier–Stokes equations are

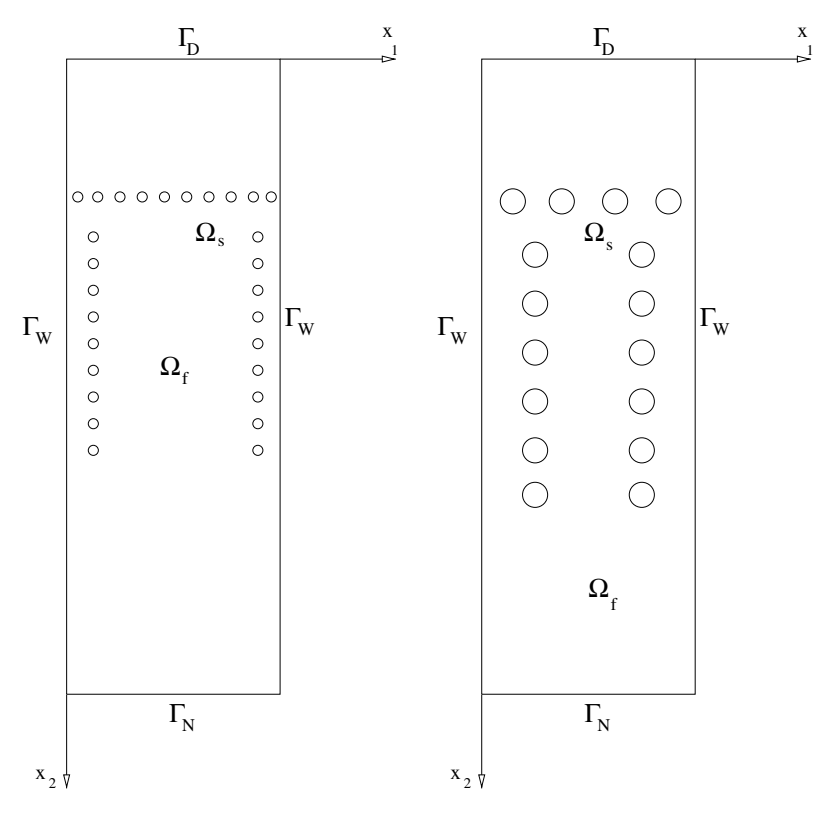


Fig. 1. Numerical experiments setup.

prescribed. The boundary of  $\Omega_{\rm f}$  is defined by  $\partial\Omega_{\rm f}=\partial\Omega_{\rm s}\cup\Gamma_{\it D}\cup\Gamma_{\it W}\cup\Gamma_{\it N}$ . A non homogeneous Dirichlet boundary condition, namely a Poiseuille flow, is imposed at the entrance section  $\Gamma_{\it D}$  and a no-slip boundary condition is specified on the walls  $\Gamma_{\it W}$ . The solid obstacles are considered like a porous medium of very low permeability and taken into account by a  $L^2$  penalization procedure which consists in adding a penalization term  $U/\kappa$  in the equations which are now set on the whole domain  $\Omega$  [22]. Let  $\sigma$  be the stress tensor defined by

$$\sigma(U, p) = \frac{1}{Re} (\nabla U + \nabla U^t) - pI, \tag{18}$$

where  $\it I$  is the identity tensor, we have to solve the following initial boundary value problem for the primitive variables  $\it (U,p)$  as unknowns

$$\begin{split} &\partial_t U + (U \cdot \nabla) U - \operatorname{div} \sigma(U, p) + \frac{1}{\kappa} U = 0 \quad \text{in } \Omega_T = \Omega \times (0, T), \\ &\operatorname{div} U = 0 \quad \text{in } \Omega_T, \\ &U(\boldsymbol{x}, 0) = U_0(\boldsymbol{x}) \quad \text{in } \Omega, \\ &U = U_D \quad \text{on } \Gamma_D \times (0, T), \\ &U = 0 \quad \text{on } \Gamma_W \times (0, T), \\ &\sigma(U, p) \cdot n + \frac{1}{2} (U \cdot n)^- (U - U^{\text{ref}}) = \sigma(U^{\text{ref}}, p^{\text{ref}}) \cdot n \quad \text{on } \Gamma_N, \end{split} \tag{19}$$

where  $U_0$  stands for the initial datum,  $U_D$  for the Poiseuille flow and  $(U^{\mathrm{ref}}, p^{\mathrm{ref}})$  for a reference flow that is supposed to have the same traction at the exit section than the studied flow [23]. In this Brinkman–Navier–Stokes model, the scalar function  $\kappa$  is the non-dimensional permeability coefficient of the porous medium. In the fluid domain  $\kappa$  goes to infinity and the penalization term vanishes to get the Navier–Stokes equations while in the solid domain  $\kappa$  goes to zero and the Darcy equations are recovered [22]. For numerical experiments we set  $\kappa=10^{-8}$  in the cylinders and  $\kappa=10^{16}$  elsewhere. This problem (19) has been theoretically studied in [24].

The equations are discretized in time by a second-order Gear scheme with an implicit treatment of the linear terms and an explicit treatment of the convection term. The spatial approximation is performed on uniform staggered grids using second-order centered finite differences for the linear terms and a third-order upwind scheme for the convection term [25]. The location of the unknowns enforce the divergence-free equation which is discretized on the pressure points and the choice of uniform grids is necessary to maintain the accuracy of the finite differences schemes. The whole problem is solved by a multigrid method with a cell by cell Gauss–Seidel iterative procedure as smoother. A sequence of grid from  $4\times 16$  cells up to  $1024\times 4096$  cells or from  $5\times 20$  cells up to  $640\times 2560$  cells is used on the domain  $\Omega=(0,1)\times (0,4)$  to get accurate results.

# 3.3. The filtering process

The theory concerning the wavelet packets has been detailed in [6] and will not be repeated here. The same Daubechies type wavelets are used in the current paper to build the packets array, and the entropy criterion is used in the best basis selection process. In [6], a few tests were performed in order to get the best wavelet mother, and to determine the number of scales necessary for an efficient representation of the flow. The criterion was then the minimization of the entropy. It had been shown that it was not necessary to perform the wavelet packets decomposition over more than 3 scales when the finest scale corresponds to a  $320 \times 1280$  grid. It has to be reminded here that the scale sequence goes from finest scales to coarsest scales. It leads to the most efficient representation according to the entropy criterion but not to the smoothest fields after filtering. Indeed, to smooth the discontinuities, it is necessary to go over at least 4 scales for such a grid [10]. That means that in [6], where only 3 scales were considered, some spurious coefficients due to the discontinuities remained in the spectra, and the slopes detected in the figures were partly altered. So in this paper, all the decompositions have been performed over 5 scales for a  $640 \times 2560$  or a  $1024 \times 4096$  grid.

The overall filtering process can be summarized as follows:

- (1) Computation of the wavelet packets decomposition of the two components of the velocity  $U = (u_1, u_2)$  over 5 scales.
- (2) Separation of the velocity fields into two subfields: the first subfield  $U_s = (u_{1s}, u_{2s})$  corresponds to the wavelet packet coefficients with a modulus larger than a given threshold  $\epsilon$ , and the second one  $U_f = (u_{1f}, u_{2f})$  corresponds to the wavelet packet coefficients with a modulus smaller than  $\epsilon$ .
- (3) Construction of the corresponding vorticity fields,  $\omega_s$  and  $\omega_f$ . The filtered field  $\omega_s$  is then essentially composed by the solid rotation part of the vortices, and the filtered field  $\omega_f$  by the vorticity filaments in between that roll-up in spirals inside the vortices.
- (4) Computations of the physical data: energy and enstrophy spectra and fluxes.

# 4. Numerical pitfalls in windowing process and filtering methods

A snapshot of the vorticity field in the wake of the cylinders for the first numerical experiment setup of Fig. 1 is plotted in Fig. 2. To compute the energy and enstrophy spectra, we select the square of size L=1 located at the end of the channel (delimited by a thin dotted line in Fig. 2) as domain of analysis.

## 4.1. Numerical pitfalls in windowing process

The cutting process to select this domain creates many discontinuities in the velocity and vorticity fields at the boundaries, and thus introduces essentially high frequency coefficients in Fourier space. This phenomenon, well known from people using the classical FFT algorithm, is described in [26,27] but its negative consequence for interpreting the two-dimensional turbulence spectra has never been enlightened. One can avoid this problem by using a windowed Fourier transform that removes the spurious coefficients created by the discontinuities. Some of the windows generally used, as the Hanning window often applied in energy spectrum computations, remove a significant part of the energy and enstrophy contained in the fields.

The Tukey windows use a parameter allowing to vary the size of the horizontal plateau in order to increase the percentage of the energy kept in the analysis process. The resulting energy spectra computed using such windows on the coarse mesh of  $320 \times 1280$  cells are shown in Fig. 3. It can be noticed that the slope detected between  $k \approx 10$  and  $k \approx 70$  is the same for the Hanning, Tukey (0.5) and Tukey (0.1) windows. The three curves are parallel and

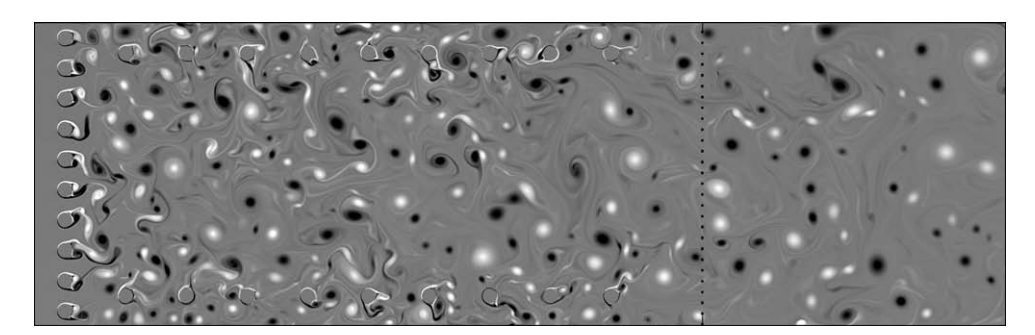


Fig. 2. Snapshot of the vorticity field with the selected domain of analysis at the end of the channel delimited by a dotted line.

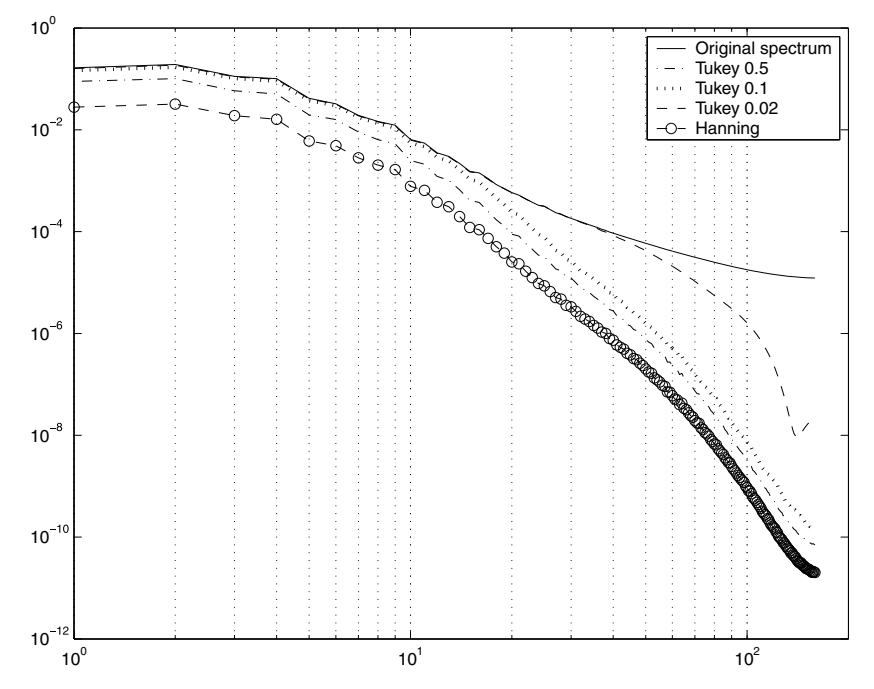
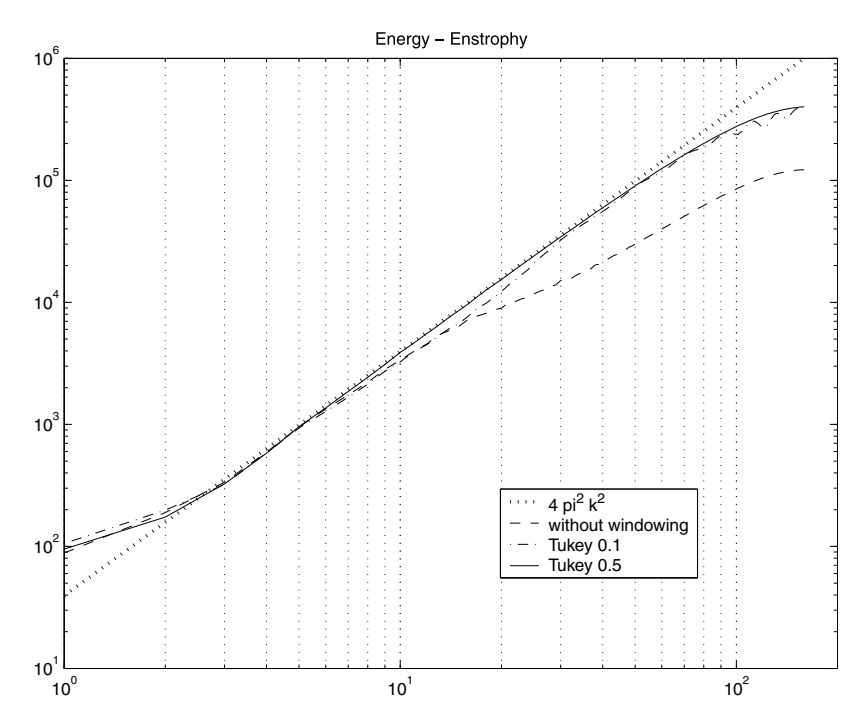


Fig. 3. Various windowed energy spectra.



**Fig. 4.** Windowed average Z(k)/E(k).

the only difference is the level of energy kept by the windowing process. The best level is given by a Tukey window with a quite small parameter equal to 0.1. A Tukey window with a larger plateau (smaller parameter equal to 0.02 for instance) does not smooth enough the discontinuities and the spectrum is closer to the non windowed spectrum which is completely wrong beyond the injection scale. The first bound of this slope is close to the injection scale while the second bound is linked to the grid, the finer the computational grid is the larger this bound is. The energy decrease is around  $k^{-5.5}$  and so far from the KLB theory that predicts a decrease in  $k^{-3}$ . But the simulations correspond to a real flow in a bounded domain with various boundary conditions completely different from the periodic case.

These results show that the discontinuities alter drastically the energy or enstrophy spectra by generating many spurious coefficients not linked to the real frequency content. They show also that some windows like Hanning window are relevant to compute the spectra but can not be used for other purposes like the computation of the fluxes as they cancel a too large amount of the energy or the enstrophy.

Computing the energy and enstrophy spectra in the selected domain of analysis, one can check the validity of the relation (13) which writes

$$Z(k) = 4\pi^2 k^2 E(k) \tag{20}$$

in our case.

The results show that without windowing the results are not correct and the relation above is satisfied only in a range from  $k\approx 2$  to  $k\approx 20$  (see Fig. 4 where the average ratio Z(k)/E(k) is plotted). The first bound corresponds to the biggest possible structure and the second bound to the injection scale. Once again these results show the need of windowing to get reliable results. Then the relation is satisfied in the whole significant spectrum where the upper bound can be pushed forward using a finer approximation as it corresponds to the smaller structures captured on the given mesh. The curve for the Hanning windowing has not been reproduced in Fig. 4 since it was exactly the same as for the Tukey (0.5) windowing.

#### 4.2. Numerical pitfalls in filtering methods

We have discussed in the previous subsection the effects of the discontinuities created by the selection of a domain of analysis within a velocity or vorticity field. Here we focus on the discontinuities created by a filtering process allowing to separate the vortices from the vorticity filaments. The goal of the present section is to reveal the real frequency content of the filtered fields. A cut-off filtering and a wavelet packet decomposition are considered in the sequel. All the computations in this section have been performed on a  $640 \times 2560$  grid.

It is shown in Fig. 5 the two cut-off filtered vorticity fields corresponding to the particular snapshot studied. This cut-off filtering is done directly on the vorticity function splitted into two parts according to a chosen threshold. For a good threshold the vortices are clearly extracted from the whole flow, the remaining is the complementary part with the background showing vorticity filaments. The vortices and the filaments fields, as described in [9], should lead to different energy spectra. The average energy spectra computed with 80 snapshots for the filtered fields are plotted in Fig. 6. According to the previous section, these spectra are computed using a windowed Fourier transform with a Tukey (0.1) window to remove the spurious coefficients generated by the boundary conditions. As expected, the spectrum of the fields with only the vortices does not present the same decrease as the spectrum of the filaments fields. A slope around -3 is observed for the vortices, and around -5/3 for the filaments before the injection scale. The theoretical value of -5/3 has been explained by Vassilicos and Hunt, and numerically observed by Borue. However, if one carefully observes the spectra, one can notice that both fields have the same behavior from the injection scale  $k_{ini} = 20$  to the end of the spectra. This range is exactly the same as the one enlightened in the previous section. But here the slopes observed in this range are only due to the discontinuities created by the filtering process instead of the boundary cutting. So it is not surprising that both fields present the same behavior in this spectral range since the discontinuities are the same in both filtered fields. In order to better understand the phenomenon, we propose to study the problem

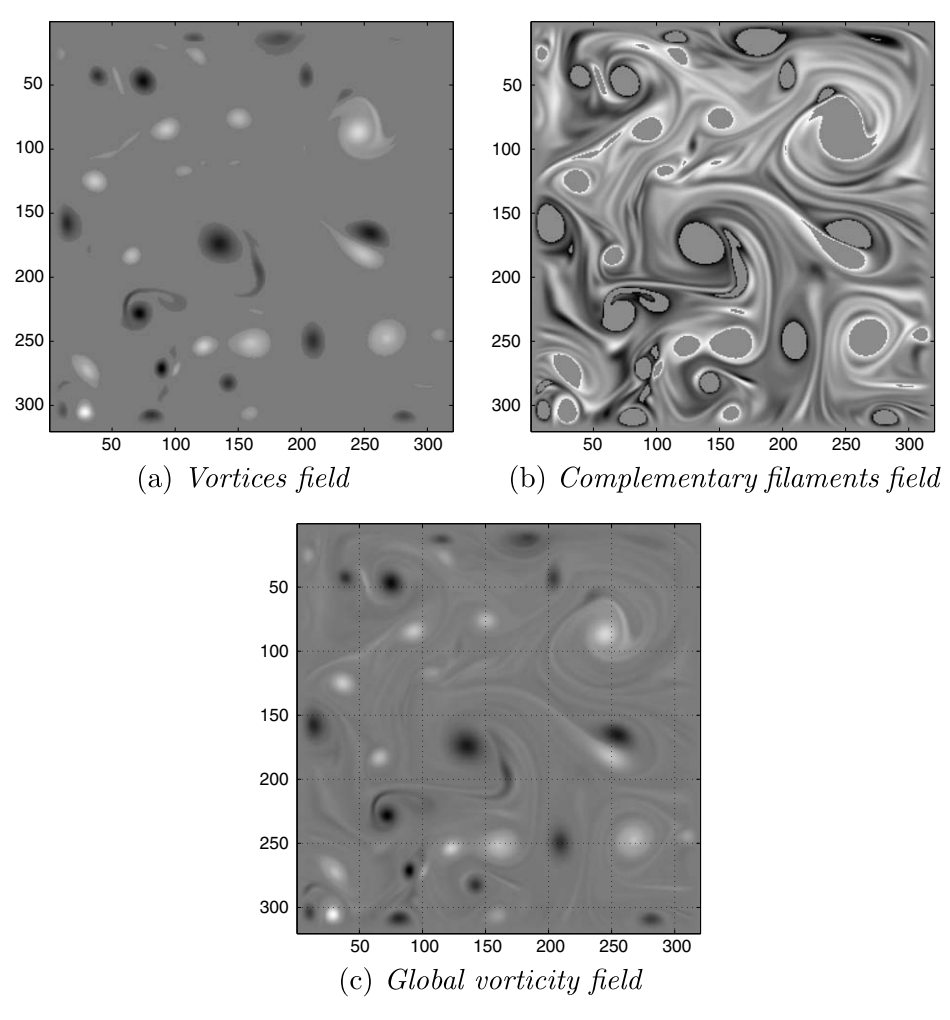


**Fig. 5.** Cut-off filtering of a snapshot at the end of the channel  $(k_{\rm inj} \approx 20)$ .

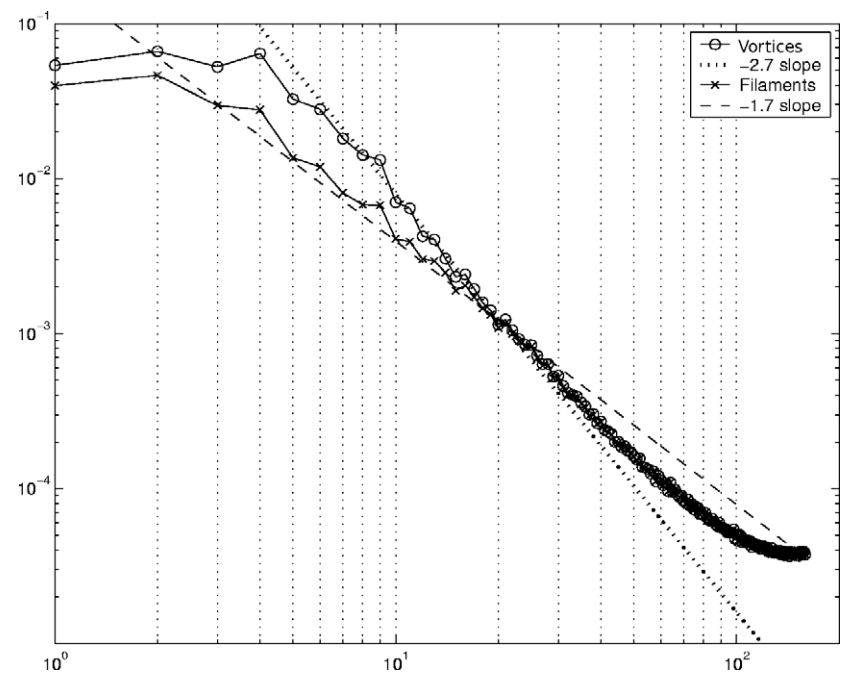


Fig. 6. Energy spectra obtained thanks to a cut-off filtering.

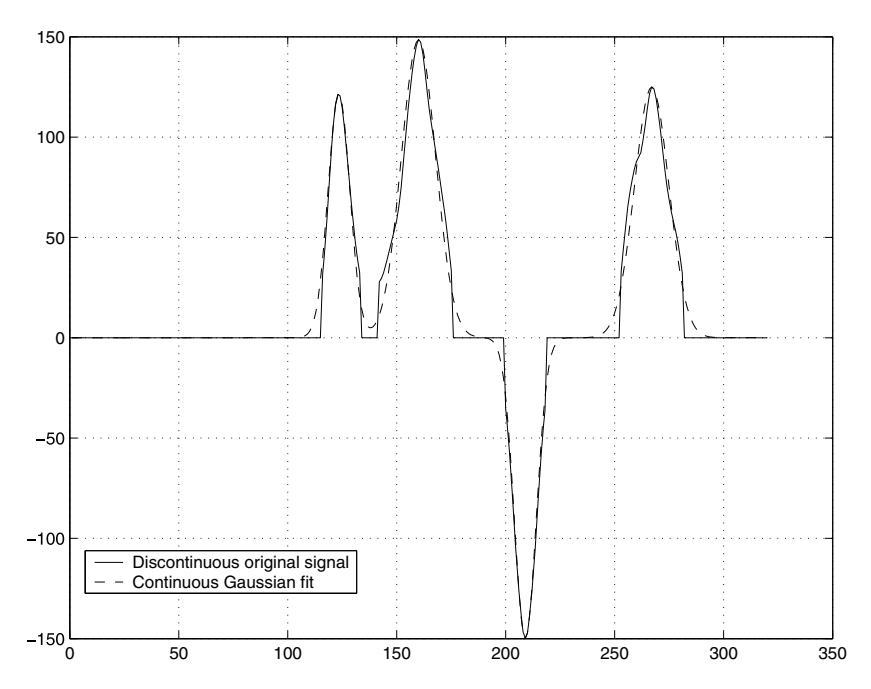


Fig. 7. Gaussian fit of the one-dimensional cut.

on a one-dimensional cut of the field located for instance along the row 250 of the global vorticity field of Fig. 5. This one-dimensional curve is plotted in Fig. 7. This cut contains four vortices, and the corresponding one-dimensional Fourier spectrum is given in Fig. 8. This spectrum is obviously very noisy since it has been computed with only one signal. To remove the discontinuities, we can use a continuous Gaussian fit of the signal very close to the original cut as seen in Fig. 7. The main difference between these two curves is the smoothing of the discontinuities. One can compare the spectrum of the Gaussian fit to the spectrum of the original cut previously computed (see Fig. 8). Both spectra are identical in the beginning of the frequency range and differ only from the injection

scale, where the continuous approximation spectrum presents a very fast decay to zero as expected as there are no high frequencies in the signal. The conclusion is that many spurious coefficients due to the discontinuities are hiding the real spectral behavior beyond the injection scale and consequently the direct enstrophy cascade cannot be studied properly. The same phenomenon obviously occurs during the computation of two-dimensional spectra of filtered fields. A nice solution to avoid this problem consists in substituting a smooth filtering wavelet packets decomposition to the discontinuous cut-off process.

This section mainly points out two technical pitfalls when computing energy or enstrophy spectra and filtering velocity or vortic-

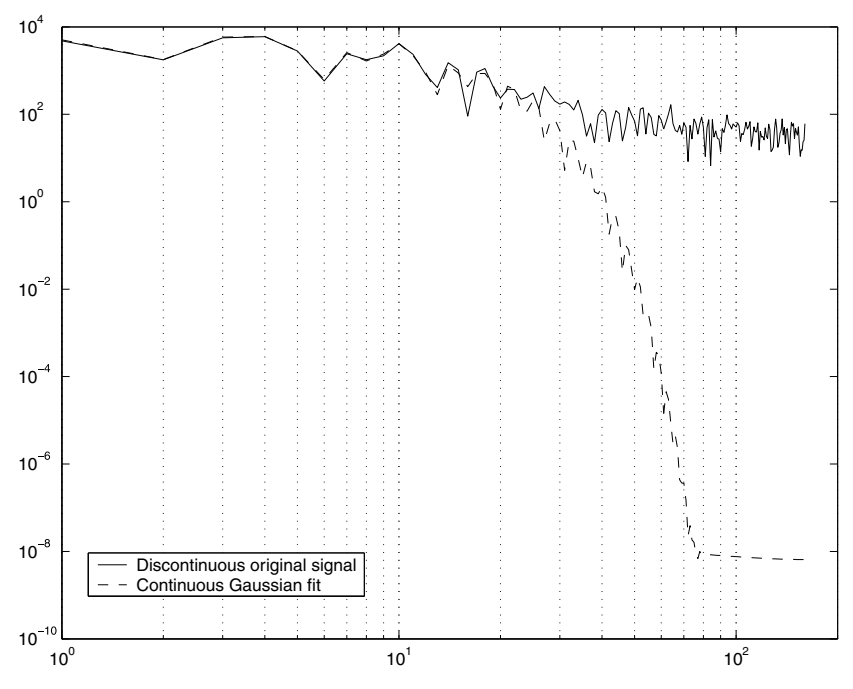


Fig. 8. One-dimensional cut spectra.

ity fields. These pitfalls can lead to a misinterpretation of the physical contents. Of course the above discussion does not affect the results of the literature in the periodic case or in the non periodic case when a window is properly used but could affect some results obtained with a discontinuous filtering.

#### 5. Computation of the physical spectra and fluxes

In this section is presented the main result of the paper concerning the analysis of the role of each filtered subfield to the two-dimensional turbulence mechanism.

#### 5.1. Computation of the energy and enstrophy spectra

The velocity decomposition  $U = U_s + U_f$  obtained with the wavelet packets based filtering is orthogonal and leads to the energy spectrum decomposition

$$E(k) = E_{\rm S}(k) + E_{\rm f}(k),$$
 (21)

where  $E_{\rm s}$  is the energy of the solid rotation vortices and  $E_{\rm f}$  is the energy of the vorticity filaments, as can be verified in Fig. 9. We observe that both subfields are multiscale even if the  $E_{\rm s}$  spectrum dominates before the injection scale and the  $E_{\rm f}$  spectrum dominates after the injection scale. And the filtered energy spectra are superimposed to the global energy spectrum when they dominate. As the spurious coefficients due to the discontinuities have been removed by the wavelet packets filtering, a first decreased in  $k^{-2}$  and a second decreased in  $k^{-5.5}$  on both sides of the injection scale are obtained. The first slope is not really clear as it is short but the second one is obvious.

The same decomposition of the enstrophy spectrum yields a behavior in  $k^0$  and  $k^{-3.5}$ , respectively, as can be observed in Fig. 10. The decomposition into the two subfields obtained by the wavelet packets filtering process is given in Fig. 11. The solid rotation subfield  $\omega_s$  reveals all the vortices with a smooth transition and the vorticity filaments subfield  $\omega_f$  shows the vorticity filaments between the vortices that end up in spirals inside the vorti-

ces. Both subfields are continuous and multiscale. The first subfield is obtained with less than 1% of the coefficients of the decomposition. It contains more than 95% of the total energy and around 70% of the enstrophy while the second one contains less than 5% of the total energy but around 30% of the enstrophy. This share-out of the enstrophy shows that unfortunately the whole flow can not be represented properly only by the first subfield. Indeed, when the vorticity filaments subfield is neglected, the global motion cannot be correct.

# 5.2. Computation of the energy and enstrophy fluxes

We recall that the energy flux is computed from the nonlinear term in the Navier–Stokes equation written in Fourier space

$$\Pi_E(k) = \int_{k}^{+\infty} T_E(k') \, \mathrm{d}k',\tag{22}$$

where  $T_E(k)$  is the nonlinear energy transfer function, and is obtained by angular integration of  $U^*(\mathbf{k}) \cdot (U \cdot \widehat{\nabla}) \widehat{U}(\mathbf{k})$ . The enstrophy flux is obtained in the same way

$$\Pi_Z(k) = \int_k^{+\infty} T_Z(k') \, \mathrm{d}k',\tag{23}$$

where  $T_Z(k)$  is the enstrophy transfer function, and is obtained by angular integration of  $\widehat{w^*(k)} \cdot (U \cdot \widehat{\nabla}) \widehat{w}(k)$ .

The energy and enstrophy fluxes corresponding to the numerical experiments above with  $k_{inj}=20$  are, respectively, given in Figs. 12 and 13. The energy flux of the whole flow is negative for wave numbers k below the injection scale 20 and almost zero above. The enstrophy flux is on the other hand positive beyond the injection scale, and negative below. The zero crossing corresponds approximately to the injection scale. These results show the existence of leading cascades, upscales for the inverse energy cascade and downscales for the direct enstrophy cascade; but also the existence of subleading cascades as theoretically shown by Tung and Gkioulekas in [28,29,14]. Let us remark that, as the injection scale is relatively large, the energy cascade cannot be completely developed. A priori, if the turbulence is inertial, the energy flux should present

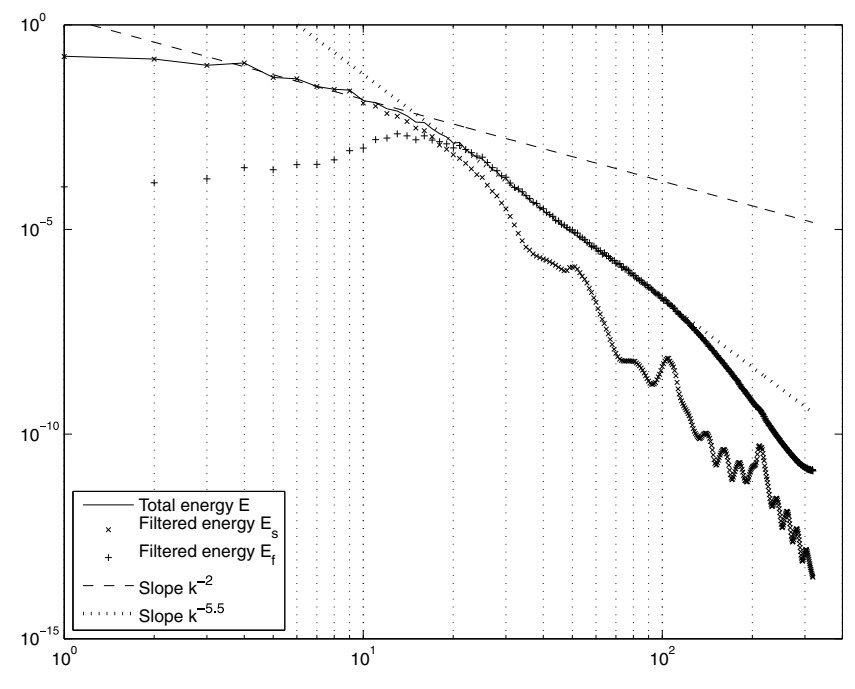
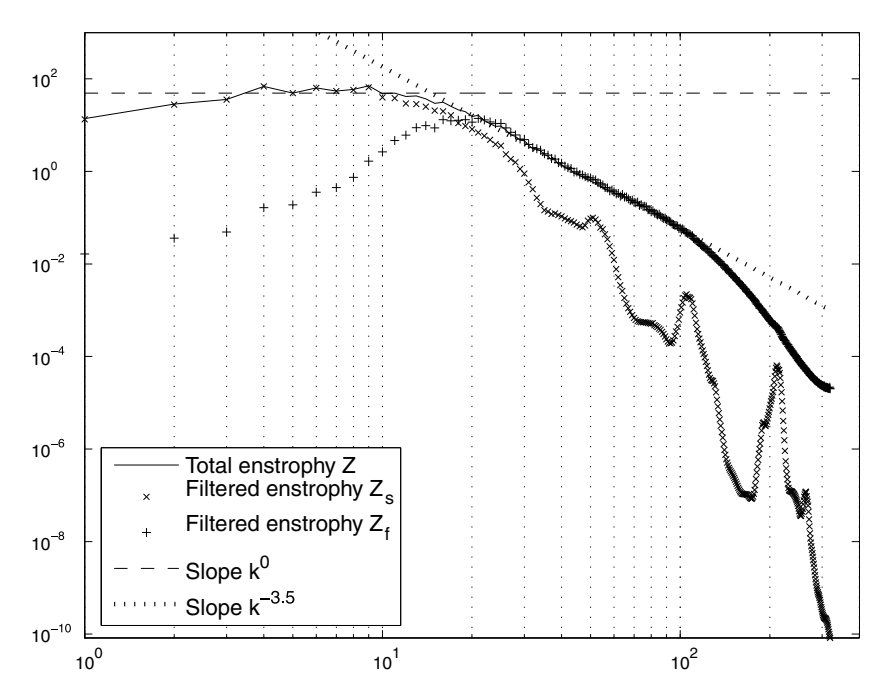
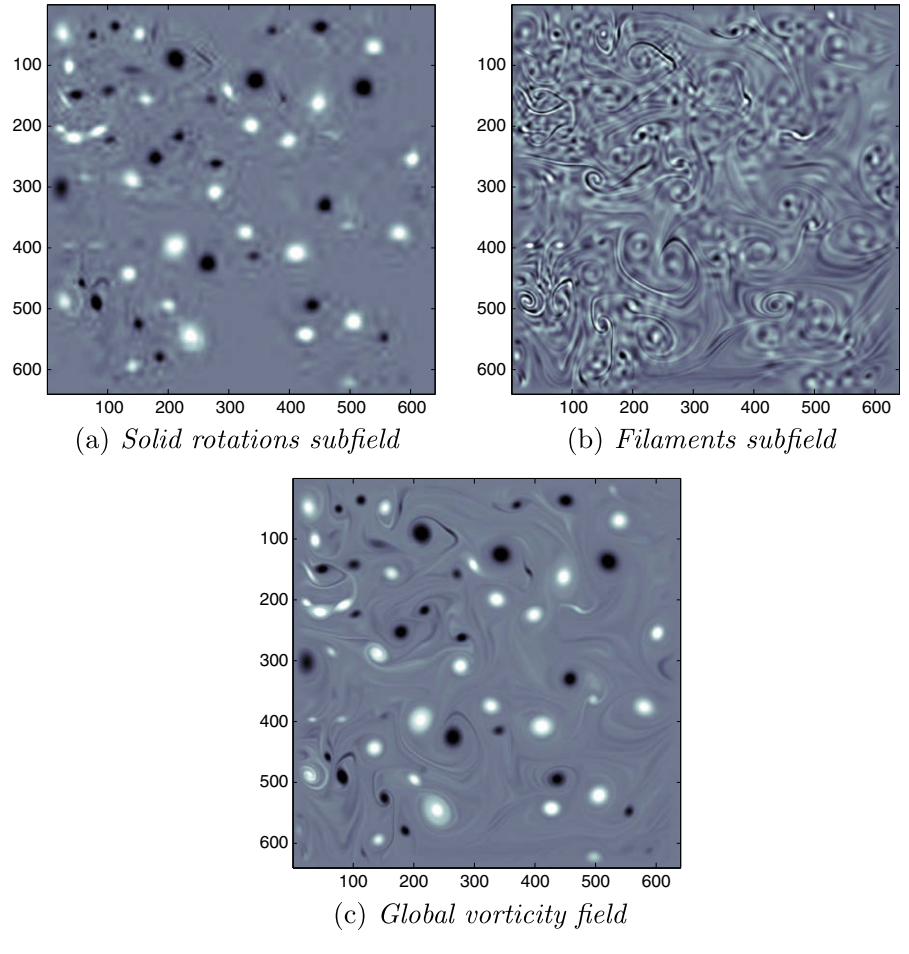


Fig. 9. Energy spectra of the original and filtered fields obtained by a 5 scales wavelet packets decomposition  $(k_{ini} \approx 20)$ .



**Fig. 10.** Original and filtered (WP 5 scales) enstrophy spectra  $(k_{inj} \approx 20)$ .



**Fig. 11.** Wavelet packets filtering of a snapshot at the end of the channel  $(k_{inj} \approx 20)$ .

a plateau in the small wave number range. Our simulations do not produce a large plateau but an explanation for this is the limitation of the range of scales probed and the presence of the boundaries.

However, both the energy flux and the enstrophy flux show that the classical picture of 2D turbulence is valid for the flow considered.

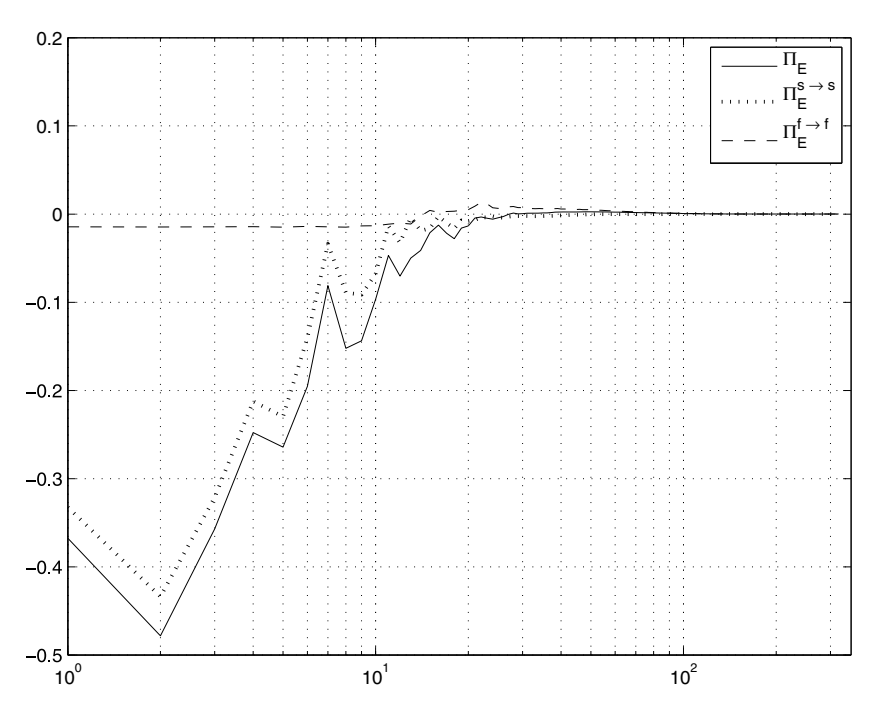


**Fig. 12.** Energy fluxes of the whole flow and of the filtered subfields  $(k_{inj} \approx 20)$ .

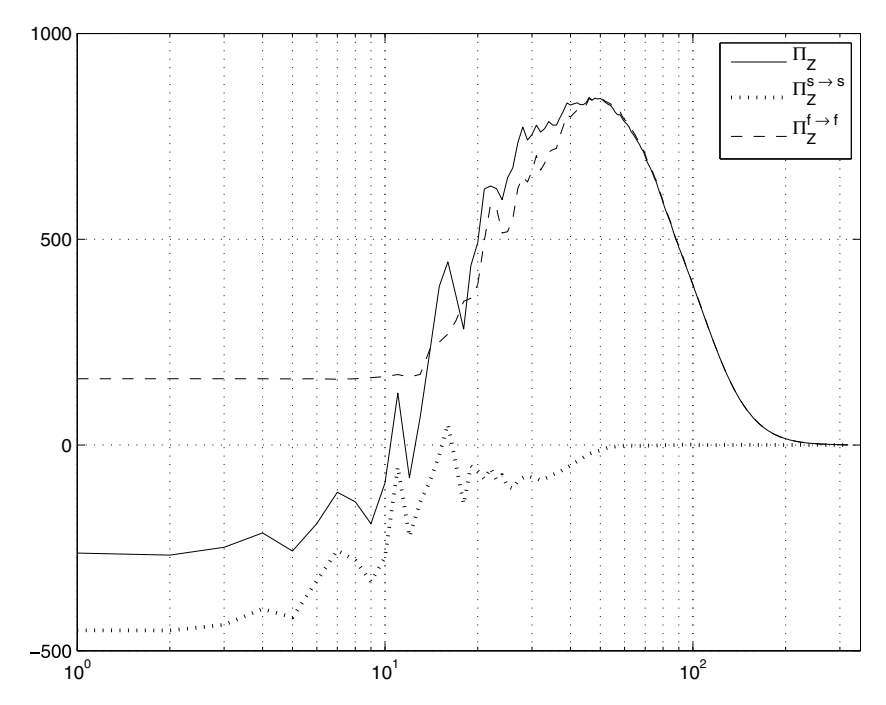


**Fig. 13.** Enstrophy fluxes of the whole flow and of the separate structures  $(k_{inj} \approx 20)$ .

In order to study in detail the energy transfer, we focus now on the nonlinear energy transfer function which, due to the orthogonal decomposition, can be written as

$$T_{E}(\mathbf{k}) = \widehat{U^{*}(\mathbf{k})} \cdot (U \cdot \widehat{\nabla}) \widehat{U}(\mathbf{k})$$

$$= \widehat{U^{*}_{s}(\mathbf{k})} \cdot (U \cdot \widehat{\nabla}) \widehat{U_{s}}(\mathbf{k}) + \widehat{U^{*}_{s}(\mathbf{k})} \cdot (U \cdot \widehat{\nabla}) \widehat{U_{f}}(\mathbf{k})$$

$$+ \widehat{U^{*}_{f}(\mathbf{k})} \cdot (U \cdot \widehat{\nabla}) \widehat{U_{s}}(\mathbf{k}) + \widehat{U^{*}_{f}(\mathbf{k})} \cdot (U \cdot \widehat{\nabla}) \widehat{U_{f}}(\mathbf{k}). \tag{24}$$

The global energy transfer can be split into four parts corresponding to the multiscale transfers from one subfield to itself or to the other one. For instance,  $\widehat{U_s}^*(\mathbf{k}) \cdot (U \cdot \widehat{\nabla}) U_f(\mathbf{k})$  is the energy

transfer from the vorticity filaments subfield to the solid rotation subfield. The fluxes corresponding to each term in the expression for the total energy transfer function will be denoted as for example  $\Pi_E^{f\to s}$  which is the flux corresponding to the transfer term previously described. In the same way, the nonlinear enstrophy transfer term is also split into four parts

$$T_{Z}(\mathbf{k}) = \widehat{\omega_{s}^{*}(\mathbf{k})} \cdot (U \cdot \widehat{\nabla})\widehat{\omega}(\mathbf{k})$$

$$= \widehat{\omega_{s}^{*}(\mathbf{k})} \cdot (U \cdot \widehat{\nabla})\widehat{\omega}_{s}(\mathbf{k}) + \widehat{\omega_{s}^{*}(\mathbf{k})} \cdot (U \cdot \widehat{\nabla})\widehat{\omega}_{f}(\mathbf{k})$$

$$+ \widehat{\omega_{f}^{*}(\mathbf{k})} \cdot (U \cdot \widehat{\nabla})\widehat{\omega}_{s}(\mathbf{k}) + \widehat{\omega_{f}^{*}(\mathbf{k})} \cdot (U \cdot \widehat{\nabla})\widehat{\omega}_{f}(\mathbf{k}).$$
(25)

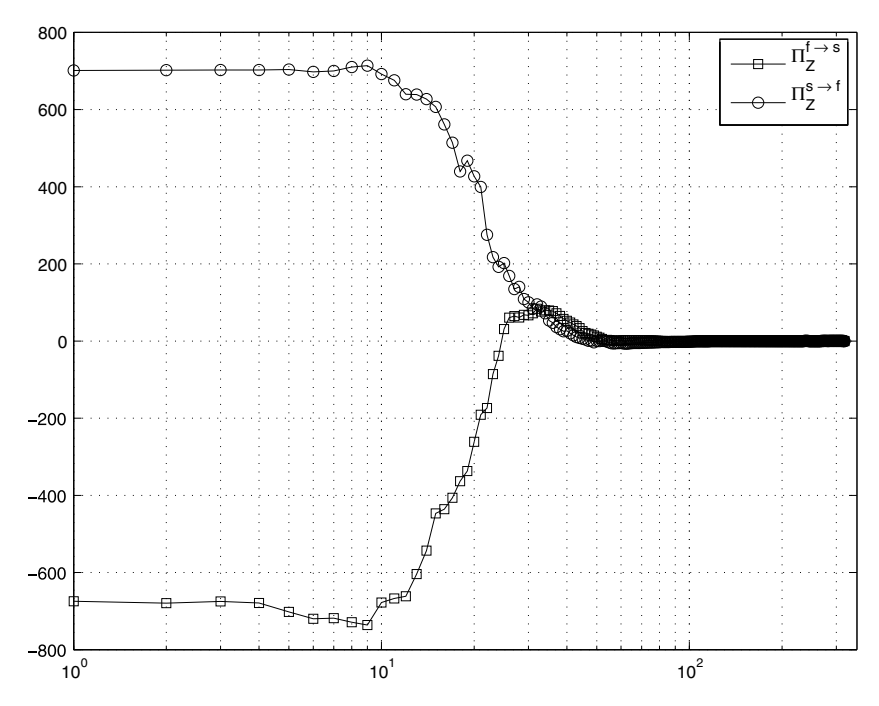


**Fig. 14.** Cross-fluxes of enstrophy  $(k_{inj} \approx 20)$ .

Using these decompositions, the fluxes associated with each structure as well as the fluxes associated with the interactions of the two structures can be obtained. Let us first consider the energy fluxes of the whole flow and of the separate structures in Fig. 12. The energy flux for the vortices shows a large negative part at small k which is similar to the total flux. The energy flux associated with the filaments is almost zero everywhere. The enstrophy flux for the vortices is negative at small k and becomes close to zero beyond the injection scale as shown in Fig. 13. The enstrophy flux for the filaments is on the other hand large and positive for the high k after the injection scale and is very close to the value of the total flux in this region of wave numbers. This preliminary examination of the fluxes indicates that the main part of the energy flux comes from the solid rotations while the main part of the enstrophy flux comes from the filamentary structures.

It is, however, possible to give a more detailed analysis of the energy and enstrophy transfers looking at the cross-fluxes. The energy flux from the vortices to the filaments and vice versa are an order of magnitude smaller than the flux due to the filaments or the flux due to the vortices. But it is shown in Fig. 14 that the cross-enstrophy fluxes  $\varPi_Z^{f \to s}$  and  $\varPi_Z^{s \to f}$  are of opposite sign and have amplitudes comparable to the total enstrophy flux. However, the sum of these two fluxes  $\Pi_Z^{f\to s} + \Pi_Z^{s\to f}$  turns out to be close to zero. While the transfer from the filaments to the vortices is negative at small k and very close to zero beyond the injection scale, the flux of enstrophy from the vortices to the filaments is positive at small kand goes to zero at high k. Concerning the enstrophy, there is a clear interaction between the two different structures. The vortices transfer enstrophy to the filaments from the large scales to the small scales up to  $k_{inj}$  while the filaments transfer enstrophy to the vortices from the injection scale to the large scales.

#### 6. Further analysis of the cascades

In order to improve the generation of each cascade separately, one can try to move the injection scale  $k_{inj}$  from one side of the spectrum to the other one. However, the possible shifts are limited due to numerical constraints. The penalization method used to

take into account the obstacles in the equations and the discretization step size do not allow the use of very small cylinders. Another interesting point is to see what are locally the events or the interactions responsible of strong energy or enstrophy transfers.

# 6.1. The inverse energy cascade

To better study the inverse energy cascade, it is useful to move the injection scale to a smaller scale, for instance by taking obstacles of size corresponding to an injection scale of  $k_{ini} \approx 40$ . The Reynolds number is still kept equal to 50,000 in these new numerical computations. The computations have been performed on a grid of size 1024 × 4096. A snapshot corresponding to this new geometry is given in Fig. 15. The statistics to compute the fluxes have been performed only on 20 snapshots in order to limit the size of the data. Consequently the fluxes are less smooth than in the previous case. The energy flux shown in Fig. 16 behaves globally like for the previous geometry. However, as expected, the inverse energy cascade has more room to take place. The energy flux tends to go to zero at the largest scales and goes back to zero close to the injection scale  $k \approx 40$  instead of  $k \approx 20$  as seen in the previous section. The energy flux of the solid rotations is very close to the global flux while the energy flux of the filaments is very low.

### 6.2. The direct enstrophy cascade

In order to study the direct enstrophy cascade, the geometry of the numerical experiment has been modified again. The turbulence is now created by three arrays of big cylinders. This setup produces an injection scale  $k_{inj}\approx 8$ . The computations have been performed on a grid of size  $512\times 2048$  for the same Reynolds number Re=50,000. A snapshot of the vorticity field corresponding to this setup is given in Fig. 17. The enstrophy flux is plotted in Fig. 18 and the global behavior is the same than for the original setup of the previous section. There is a large positive region beyond the injection scale revealing the direct enstrophy cascade. But it can also be observed a strong enstrophy transfer from the injection scale toward the largest scales linked to the inverse energy cascade. One

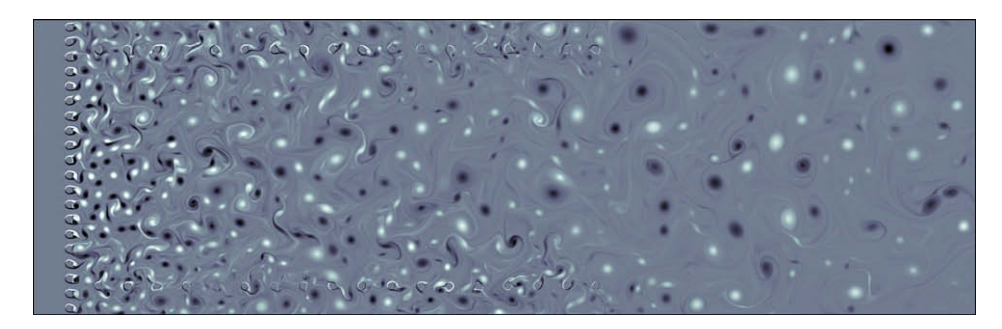
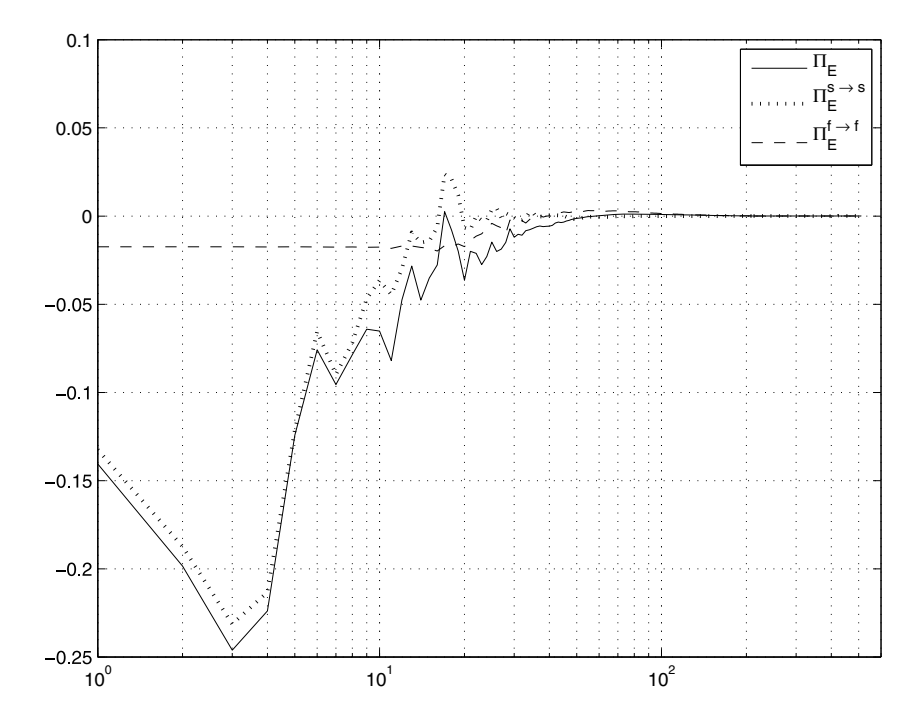


Fig. 15. Snapshot of the vorticity field.



**Fig. 16.** Energy fluxes of the whole flow and of the separate structures  $(k_{inj} \approx 40)$ .

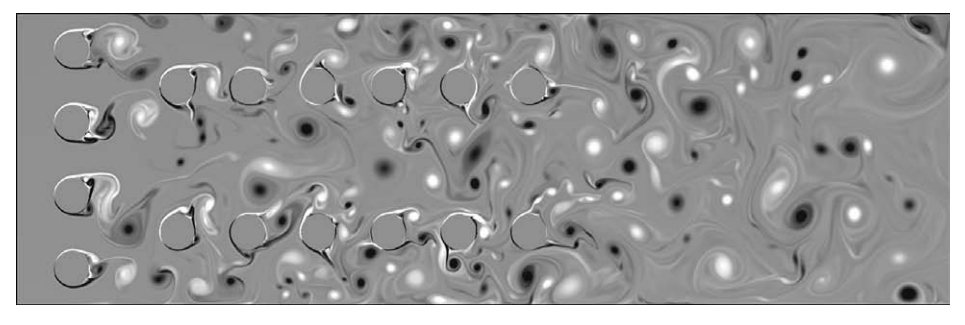
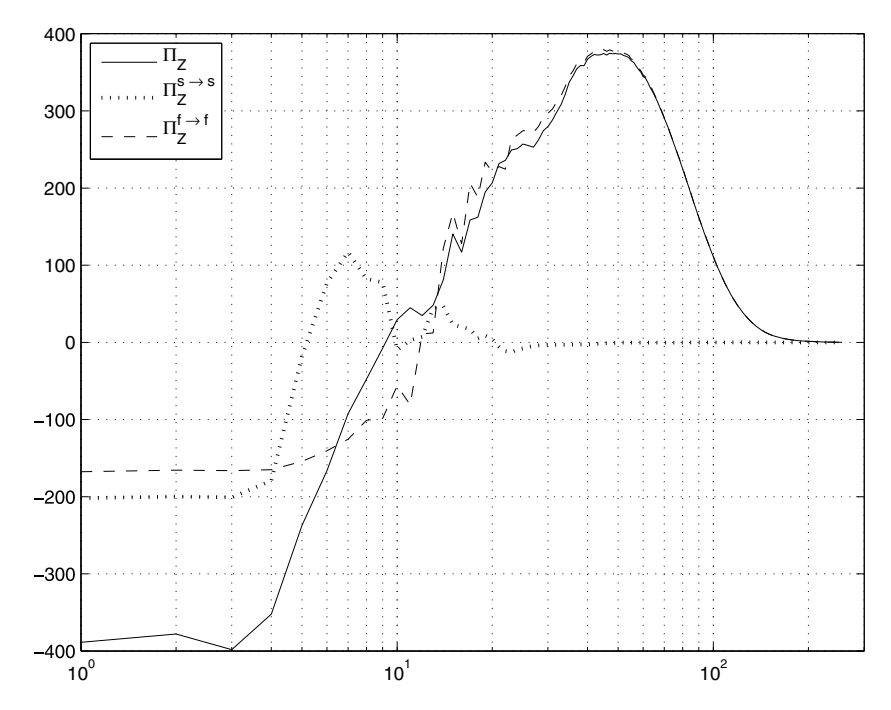


Fig. 17. Snapshot of the vorticity field.

notice again that the enstrophy flux crosses the zero axis around the injection scale. The enstrophy flux of the filaments is close to the global flux beyond the injection scale and reach another plateau for the large scales. The enstrophy flux of the solid rotations is close to zero beyond the injection scale and shows a negative plateau at large scales. The positive pic just before the injection scale should probably disappear with higher statistics. The modification of the geometry shows that the global features of the flow are always the same and proves the direct link between the diameter of the cylinders and the injection scale.

# 6.3. The local analysis

Now we have established there are two subfields that have a clear role on the turbulence cascades and that interact strongly as we have seen on Fig. 14, it is necessary to understand the mechanism of the transfers. The filamentary subfield is made of vorticity filaments that roll-up in spirals inside the vortices and so the interaction with the solid part of the vortices is obvious. Nevertheless, it is important to well understand what is going on in the strain regions. When two vortices interact, if the vortices move aside then



**Fig. 18.** Enstrophy fluxes of the whole flow and of the separate structures  $(k_{inj} \approx 8)$ .

the vorticity filament in between is stretched and if the vortices move closer then the vorticity filament in between is confined like a yo-yo. This suggests that the whole balance is zero and this is true as the sum of the cross-fluxes of enstrophy is effectively close to zero.

To have a complete understanding of the mechanisms it would be necessary to analyse each kind of structure, namely a single vortex convected and diffused by the flow without interactions, a dipole or more complex structures also convected and diffused by the flow without interactions with the rest of the flow, the merging

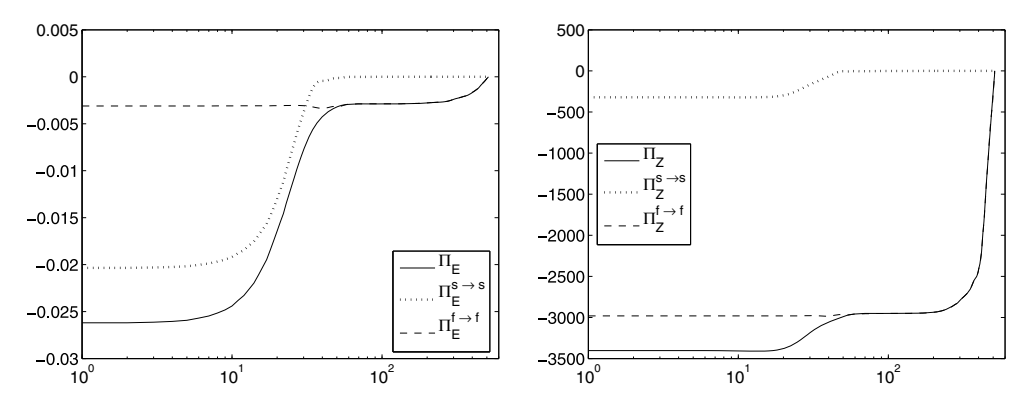


**Fig. 19.** Energy fluxes (left) and enstrophy fluxes (right) corresponding to a single vortex of diameter  $\approx L/20$ .

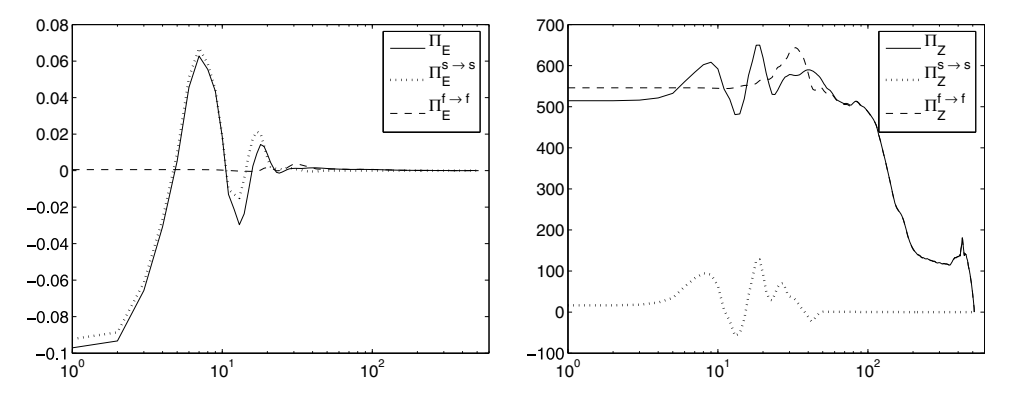


**Fig. 20.** Energy fluxes (left) and enstrophy fluxes (right) corresponding to a dipole of size  $\approx L/6$ .

of two or more vortices of the same sign, the interaction of several vortices of different sign and so on. Here, we restrict the analysis to the two first events above. To avoid numerical pitfalls, the vortex for instance is embedded into a two-dimensional Gaussian function sharing the same center. The contribution to the fluxes of such a single vortex is plotted in Fig. 19, it is in accordance with the global result for the inverse energy cascade but not for the direct enstrophy cascade as the enstrophy flux is strongly negative all way long. The same fluxes are plotted on Fig. 20 for a single dipole with a bigger size that does not interact with the rest of the flow. This time there is a positive maximum and the negative energy flux moves to the large scales as the size of the structure is bigger, this corresponds to what we have seen above with bigger cylinders. But now the enstrophy flux is always positive. In both cases we see that the solid rotation subfield follows the total field for the energy whereas the filamentary subfield follows the total field for the enstrophy and the contribution of the other subfield is very low. Repeated analysis of these two events gives always the same kind of results. The total flux for one snapshot is the sum of the local fluxes corresponding to the various structures that compose the flow.

#### 7. Conclusions

Good direct numerical simulations give a realistic approximation of two-dimensional turbulent flows corresponding to soap film experiments. The flows perturbed by arrays of cylinders reveal an injection scale directly linked to the diameter of the cylinders.

A careful analysis of the flows using wavelet packets filtering on sufficient levels yields relevant results one can trust. Using an adapted threshold on the wavelet coefficients allows to separate the flow into two continuous and multiscale subfields, on one hand the solid rotation of the vortices and on the other hand the vorticity filaments that connect the vortices and roll-up in spirals inside the vortices. The second subfield cannot be neglected as it contains around 30% of the enstrophy and contributes for a significant part of the motion of the whole flow.

The computation of energy and enstrophy spectra and fluxes reveal that the first subfield contributes significantly to the inverse energy cascade while the second subfield contributes significantly to the direct enstrophy cascade. Further local analysis should reveal the contribution of the various structures to the global dynamics.

## References

- [1] Farge M, Goirand E, Meyer Y, Pascal F, Wickerhauser M. Improved predictability of two-dimensional turbulent flows using wavelet packet compression. Fluid Dyn Res 1992;10:229–50.
- [2] Farge M, Holschneider M, Colonna JF. Wavelet analysis of coherent structures in two-dimensional turbulent flows. In: Moffatt HK, Tsinober A, editors.

- Topological fluid mechanics. Cambridge: Cambridge University Press; 1990. p. 765–76.
- [3] Farge M, Pellegrino G, Schneider K. Coherent vortex extraction in 3D turbulent flows using orthogonal wavelets. Phys Rev Lett 2001;87(5):45011–4.
- [4] Farge M, Schneider K, Kevlahan N. Non-Gaussianity and coherent vortex simulation for two-dimensional turbulence using an adaptative orthogonal wavelet basis. Phys Fluids 1999;11(8):2187–201.
- [5] Fischer P, Bruneau CH, Kellay H. Multiresolution analysis for 2D turbulence. Part 2: a physical interpretation. Discr Cont Dyn Syst B 2007;4:717–34.
- [6] Fischer P. Multiresolution analysis for two-dimensional turbulence. Part 1: wavelets vs cosine packets, a comparative study. Discr Cont Dyn Syst B 2005;5:659–86.
- [7] Benzi R, Patarnello S, Santangelo P. On the statistical properties of twodimensional decaying turbulence. Europhys Lett 1987;3:811–8.
- [8] Benzi R, Patarnello S, Santangelo P. Self-similar coherent structures in twodimensional decaying turbulence. J Phys A: Math Gen 1988;21:1221–37.
- [9] Borue V. Inverse energy cascade in stationary two-dimensional homogeneous turbulence. Phys Rev Lett 1994;72:1475–8.
- [10] Bruneau CH, Fischer P. Spectra and filtering: a clarification. Int J Wavelets, Multiresolution Informat Process 2007;5:465–83.
- [11] Obukhov AM. On the distribution of energy in the spectrum of turbulent flow. Dokl Akad Nauk SSSR 1941;32:22-4.
- [12] Obukhov AM. Spectral energy distribution in a turbulent flow. Izv Akad Nauk SSSR Ser Geogr Geofiz 1941;5:453–66.
- [13] Frisch U. Turbulence: the legacy of A.N. Kolmogorov. Cambridge: Cambridge University Press: 1995.
- [14] Tung KK, Gkioulekas E. Is the subdominant part of the energy spectrum due to downscale energy cascade hidden in quasi-geostrophic turbulence? Discr Cont Dyn Syst B 2007;7:293–314.
- [15] Kellay H, Goldburg WI. Two-dimensional turbulence: a review of some recent experiments. Rep Prog Phys 2002;65:845–94.
- [16] Kellay H, Wu XL, Goldburg WI. Experiments with turbulent soap films. Phys Rev Lett 1995;74:3975–8.
- [17] Rutgers M. Forced 2D turbulence: experimental evidence of simultaneous inverse energy and forward enstrophy cascades. Phys Rev Lett 1998:81:2244-7.
- [18] Rivera MK, Daniel WB, Chen SY, Ecke RE. Energy and enstrophy transfer in decaying two-dimensional turbulence. Phys Rev Lett 2003;90:104502(4).
- [19] Bruneau CH, Kellay H. Coexistence of two inertial ranges in two-dimensional turbulence. Phys Rev E 2005;71:046305(5).
- [20] Bruneau CH, Fischer P, Peter Z, Yger A. Comparison of numerical methods for the computation of energy spectra in 2D turbulence. Part I: direct methods. Samp Theory Signal Image Process 2005;4:169–92.
- [21] Bruneau CH, Fischer P, Peter Z, Yger A. Comparison of numerical methods for the computation of energy spectra in 2D turbulence. Part II: adaptative algorithms. Samp Theory Signal Image Process 2005;4:271–80.
- [22] Angot P, Bruneau CH, Fabrie P. A penalization method to take into account obstacles in incompressible viscous flow. Numer Math 1999;81(4):497–520.
- [23] Bruneau CH. Boundary conditions on artificial frontiers for incompressible and compressible Navier-Stokes equations. M2AN 2000;34(2):303–14.
- [24] Bruneau CH, Fabrie P. New efficient boundary conditions for incompressible Navier–Stokes equations: a well-posedness result. M2AN 1996;30(7):815–40.
- [25] Bruneau CH, Saad M. The 2d lid-driven cavity problem revisited. Comput Fluids 2006;35:326–48.
- [26] Press W, Teukolsky S, Vetterling W, Flannery B. Numerical recipes. Cambridge: Cambridge University Press; 2001.
- [27] Priestley M. Spectral analysis and time series. Academic Press; 1981.
- [28] Gkioulekas E, Tung KK. On the double cascades of energy and enstrophy in two-dimensional turbulence. Part 1: theoretical formulation. Discr Cont Dyn Syst B 2005;5:79–102.
- [29] Gkioulekas E, Tung KK. On the double cascades of energy and enstrophy in two-dimensional turbulence. Part 2: approach to the KLB limit and interpretation of experimental evidence. Discr Cont Dyn Syst B 2005:5:103-24